INT. J. REMOTE SENSING, 1995, VOL. 16, NO. 5, 851–876

Laboratory measurements of radar backscatter from bare and snow-covered saline ice sheets

S. G. BEAVEN, G. L. LOCKHART, S. P. GOGINENI, A. R. HOSSEINMOSTAFA

Radar Systems and Remote Sensing Laboratory, Department of Electrical Engineering and Computer Science, University of Kansas, 2291 Irving Hill Road, Lawrence, Kansas 66045-2969, U.S.A.

K. JEZEK

Byrd Polar Research Center, The Ohio State University, 108 Scott Hall, 1090 Carmack Road, Columbus, OH 43210-1002, U.S.A.

A. J. GOW, D. K. PEROVICH

U.S. Army Cold Regions Research and Engineering Laboratory, 72 Lyme Road, Hanover, NH 03755-1290, U.S.A.

A. K. FUNG and S. TJUATJA

Wave Scattering Research Center, Department of Electrical Engineering, The University of Texas, 416 Yates Street, Arlington, TX 76019-0016, U.S.A.

(Received 10 January 1994; in final form 30 June 1994)

Abstract. We performed experiments to collect radar backscatter data at K_u (13·4 GHz) and C bands (5·3 GHz) over simulated sea ice at the U.S. Army Cold Regions Research and Engineering Laboratory (CRREL) during the 1990 and 1992 winter seasons. These experiments were conducted over bare saline ice grown in an indoor tank and an outdoor pond facility. The radar data were calibrated using a complex vector calibration scheme to reduce systematic effects. In conjunction with the radar measurements we measured ice physical properties.

These measurements demonstrate that the dominant backscatter mechanism for bare saline ice is surface scattering. Both the copolarized and cross-polarized measurements compare favourably with the predictions of surface scattering models at two frequencies.

During the 1992 indoor tank experiment we applied four successive layers of snow (about 2·5 cm each) to the saline ice sheet after the ice thickness had reached about 12 cm. The backscatter at normal incidence dropped by 15 dB and the backscatter at 45° increased by 11 dB with the introduction of the first snow layer. The application of three more layers, each of approximately 2·5 cm depth, did not alter the radar signature significantly. By modelling and direct observation we found that the initial change in the signature was caused by a roughening of the surface at the snow-ice interface and the change in dielectric contrast at the snow-ice interface.

1. Introduction

In 1990 and 1992 we conducted a set of carefully controlled experiments designed to measure radar backscatter from saline ice. The objective of these experiments was

to relate dominant electromagnetic scattering mechanisms to specific sea ice morphologies and physical properties through the application of forward models and empirical observations. For example, how are the dominant sources of scattering distributed in an ice sheet, and are the scatterers related to brine pockets, air pockets, or surface roughness elements? In the longer term we seek to apply specific knowledge obtained in the laboratory to answer questions about the more general condition found on the polar oceans. In particular, we would like to discriminate better between open water, new thin ice, and first-year ice using spaceborne microwave sensors because of the significant effect sea ice cover has on ocean/atmosphere heat exchange.

In this paper, we discuss analysis of data collected over thin, smooth saline ice and snow-covered ice. These are a follow-on to experiments we conducted on a urea ice sheet (Lytle *et al.* 1993). Urea-doped ice is used as a model in place of saline ice for mechanical properties testing (Timco 1980). Our work on urea ice showed that snow cover dramatically changes the backscatter response of the ice sheet via a roughening of the surface at the snow-ice interface. Hence, a key objective of the work discussed in this paper was to verify that the same physical properties and electromagnetic processes were operative in saline ice. In these experiments we also addressed the more difficult problem of isolating the dominant scattering mechanisms associated with bare saline ice.

In this paper we present the experimental methods used to quantify the radar backscatter and geophysical parameter estimates. We use these experimental results, along with forward scattering models, to determine the dominant backscatter processes for young bare and snow-covered saline ice.

The radar systems used are described in § 2 and a description of the experiments is given in § 3. In § 4 we address the surface roughness measurements and the effect of noise on the measures of roughness and correlation length. In § 5 we outline the data processing procedures used to compute the backscattering coefficient (σ°) from radar measurements. The backscatter results are presented in § 6 for both snow-covered and bare saline ice. These data are compared with surface and volume scattering models in § 7. The findings from these comparisons are then discussed in § 8.

2. Step-frequency radar systems description

We used two Vector Network Analyser (VNA)-based step frequency radars to measure backscatter from saline ice at *C* and K_u bands. The VNA plays the role of the signal generator and processor. It is used to measure coherently the amplitude and phase of the return signal (i.e., the S_{21} scattering parameter) at baseband for a set of discrete frequencies. The frequency of the network analyser is stepped through 1000 MHz of bandwidth for the K_u-band radar and 500 MHz of bandwidth for the *C*-band radar in 2·5 MHz steps. The network analyser is used to measure the return independently at each frequency, and these measurements are stored on disks through the use of a 386 computer. The radar specifications are given in table 1. The details of the operation of step-frequency radars can be found in the literature (Iizuka and Freundorfer 1984). To compute the scattering coefficient we took an inverse FFT of the measured data to determine power return as a function of range from the radar. These transformed data are then range-gated to obtain the power returned from the target.

Each system measures backscatter for all four linear polarizations (*VV*, *HH*, *VH*, *HV*). The *C*-band system uses four pyramidal horn antennas to obtain the four

polarizations. The K_u-band system consists of one diagonal horn antenna for transmitting and an identical antenna for receiving. The two polarizations are obtained through the use of orthomode transducers for each of these antennas. The diagonal horn antenna relies on the superposition of the TE_{01} and TE_{10} modes. In the diagonal horn these modes generate a field pattern that resembles the TE_{11} mode of a circular waveguide. Ideally, there is no cross-polarized pattern in the principal planes. In the 45° plane the theoretical cross-polarized pattern is about 15 dB below the normal antenna pattern near the main lobe in the ideal case (Love 1962). This is important when considering cross-polarized measurements and the effect of cross-talk between orthogonally polarized channels.

A microcomputer controls the VNA via a Hewlett Packard Interface Bus (HPIB) expansion card. A computer program controls the stepping of the VNA through the frequencies needed to produce the bandwidths shown in table 1. The program also obtains the S_{21} measurement from the VNA and stores the data to disks. The switching network, which is used to switch between polarizations, was manually controlled by an external control box.

3. CRREL experiment (CRRELEX) description

To study the mechanisms responsible for the backscatter from young sea ice we took measurements over bare and snow-covered saline ice at the U.S. Army Cold Regions Research and Engineering Laboratory (CRREL) during the winter seasons of 1990 and 1992. Saline ice sheets grown at the CRREL facility possess physical properties, such as salinity and crystalline structure, which closely simulate thin Arctic sea ice (Arcone *et al.* 1986, Gow 1986, Swift *et al.* 1992).

Radar backscatter from bare saline ice was measured at *C* band (5·3 GHz) and K_u band (13·4 GHz) during the 1990 winter season at an outdoor pond facility at CRREL. K_u-band measurements from saline ice were also performed in CRREL's indoor pit facility during the 1992 campaign. In both cases step-frequency radar systems were used to perform the measurements at all four linear polarizations (*VV*, *HH*, *VH*, *HV*).

Table 1. RSL *C*-band and K_u-band step-frequency radar specifications.

	C-band system	K_u-band system
Centre frequency	5·3 GHz	13·4 GHz
RF bandwidth	500 MHz	1 GHz
Number of samples	201	401
Range resolution in air	30 cm	15 cm
Transmitted power	10 dBm	10 dBm
IF frequency	1·7–1·2 GHz	1·5–2·5 GHz
Antennas	Type: Horn	Type: Diagonal Horn
	Beamwidth: 15° (one way)	*Beamwidth*: 8·4° (one way)
Polarizations	*VV*, *HH*, *VH*, *HV*	
Calibration	*Internal*: delay line *External*: sphere, Luneburg lens, dihedral (1990 only)	
Data acquisition	HP8753C Network analyser and zenith '386 personal computer	

3.1. *CRRELEX'90 description*

Radar backscatter measurements from artificial sea ice were made at CRREL's lower pond facility during January and March 1990. The experiment utilized an outdoor pond in which saline water of salinity 24 parts per thousand was frozen to simulate Arctic sea ice. The lower pond is made of concrete and is about 10 m × 10 m × 1·3 m, with vertical sides. The facility has a walkway mounted on tracks and served as a mobile base on which the antenna was installed. The RF sections were placed on the antenna mounts, while the data acquisition and control systems were housed in a shed adjacent to the pond. Measurements were made at incidence angles ranging from 0° to 60° at the lower pond, with all four linear polarization combinations. During this experiment, measurements were performed for ice that had grown to about 20 cm thickness. Movement of the antenna mount allowed for up to four independent spots to reduce fading, which occurs in radar backscatter measurements. Ice characterization data included roughness information obtained from photographs of thick sections. Radar backscatter measurements and ice property measurements were made in January and again in March under a variety of weather conditions.

In addition to the backscatter measurements from saline ice the radar returns from several calibration targets were measured. These targets included a Luneburg lens, a metal sphere, and a dihedral corner reflector. These measurements were made so that careful calibration could be used to remove the systematic errors. These errors are caused by signal leakage due to the system's finite polarization ratio and other effects that occur when using real antennas.

3.2. *CRRELEX'92 description*

The 1992 experiments at CRREL were performed in an indoor refrigerated facility accessible through three gasket-sealed doors. This facility is approximately 6 m × 6 m × 7 m and is divided into two levels by a steel grate. The test tank, or pit, is located in the lower level and measures approximately 5 m × 6 m × 1·5 m. The tank was filled with saline water of 24 parts per thousand salinity. Two *I*-beams, running the length of the tank slightly above water level, divide the tank into three sections. These *I*-beams provide easy access to the tank and to the radar that was mounted on another *I*-beam located directly beneath the grating. The experiment consisted of two phases as indicated below.

3.2.1. *Early growth process*

The first phase involved monitoring the change in backscatter during the early growth process. Initially, we took backscatter measurements over smooth open water. Then, the water was allowed to freeze spontaneously, without seeding, and we measured the backscatter as the ice grew. At the end of three days the ice had reached a thickness of approximately 12 cm. We took backscatter measurements during this growth process at incidence angles of 0° to 55°. Also, we periodically took transects at 0° incidence to determine the uniformity of the ice sheet in terms of the radar signature.

3.2.2. *Snow cover experiments*

In addition to the bare ice and ice growth studies we performed measurements to study the effect of snow on the radar backscatter from saline ice. Snow cover plays an important role in the thermodynamics of sea ice (Tucker *et al.* 1992). When a

snow cover is present over sea ice it acts both as a thermal insulator and as a mechanical load. This combination causes the release of brine from just below the snow-ice interface. These changes at the snow-ice interface cause significant changes in the radar signature of sea ice.

To quantify the effects of snow cover on the radar backscatter of sea ice, we made K_u-band radar backscatter measurements at CRREL's indoor pit during the 1992 experiment. After the ice grew to a thickness of 12 cm, several snow layers were piled on top of the ice to begin the second phase of the experiment. Four snow layers were applied in approximately equal increments to a height of 12 cm. These layers were made by taking newly-fallen snow from outside the CRREL facility and sifting it through a screen onto the ice to simulate a snowfall. We took backscatter measurements for each successive layer of snow added at incidence angles ranging from 0° to 55°. Finally, more snow was added to increase the average depth to 21 cm. We took backscatter measurements at this thickness at normal incidence. The radar system has a resolution of 15 cm in free space and 11 cm in the snow, due to the higher dielectric constant, so the return from the snow-ice interface is resolvable from the air-snow interface. We placed a metal plate on top of the snow to determine the range to the air-snow interface as a reference plane for the deep snow measurement.

3.3. *Saline ice and snow property measurements*

Saline ice and snow physical properties were measured in conjunction with the radar backscatter measurements. Parameters measured were surface roughness, air temperature, snow depth and density, and vertical profiles of ice temperature, salinity, brine volume, and crystal structure. Surface roughness measurements are described in §4. All other ice properties measured are summarized below.

3.3.1. *CRRELEX'92 indoor pit experiment*

Saline ice grown at CRREL's indoor pit simulates thin sea ice as is observed in the polar oceans (Swift *et al.* 1992). A collection of thin section photographs is shown here in figure 1. The photographs, taken between crossed polarizers to enhance the structure of the ice, demonstrate that the microscale properties of the saline ice are identical to sea ice. These photographs were made from samples taken at two stages of the ice growth and before snow was added to the ice sheet.

Salinity measurements were also made during the various stages of ice growth in the indoor pit. These profiles are shown in figure 2. Another thin section was taken from a saline ice sample and the brine inclusion statistics were studied by Perovich and Gow (1992). The brine pocket cross-sectional area distribution is shown here in figure 3.

In addition to the brine volume study published in Perovich and Gow (1992) a detailed study of volume scatter parameters was carried out during the winter of 1993 at CRREL's outdoor pond. Results of thin section measurements at three different depths of an ice core reveal a range of values for the brine pocket size, distribution and brine volume fraction. These results are included with salinity and temperature data in table 2. Here circularity is defined as the ratio of the brine inclusion perimeter squared, divided by the area of the brine inclusion. This gives some measure of the brine inclusion shape. Using the values for brine volume fraction and particle size we computed a range of values for the spectral albedo as demonstrated by Fung and Eom (1982). For the maximum radius we used the

maximum mean axis length. For the minimum radius we used the radius of a circle that would give the minimum mean area shown here. We found that the computed spectral albedo ranges from 0·0001 to 0·01 at K_u band and 0·00002 to 0·002 at C band.

The snow densities for the CRREL'92 indoor pit study for each of the four layers (or lifts) were measured to be 0·485, 0·277, 0·258, and 0·288 Mg m^{-3} for lifts one through four, respectively. After observing that the density of the first lift was higher than that typically observed from newly fallen snow, we sifted the snow through a

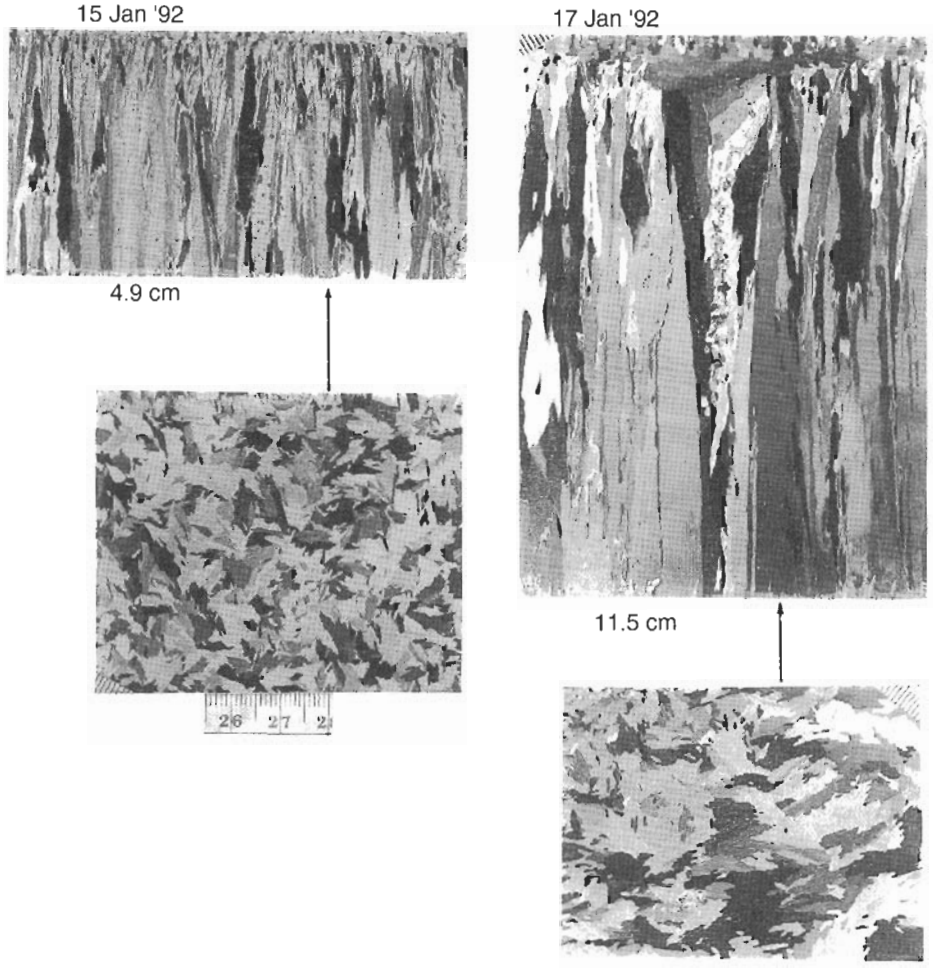

Figure 1. Vertical (top) and horizontal (bottom) thin section photographs of the ice sheet grown during CRRELEX'92 at two stages of its growth in the indoor tank. Photographs taken between crossed polarizers to reveal the elongate vertical texture of the ice crystals. Smallest scale subdivisions measure 1 mm. Rows of vertical lines in the vertical sections mark the traces of brine pocket inclusions within each crystal. Similar structures can be seen in the horizontal sections. The structure of this ice, including the arrangement of brine pockets within the crystals, replicates that observed in normal congelation (columnar) sea ice.

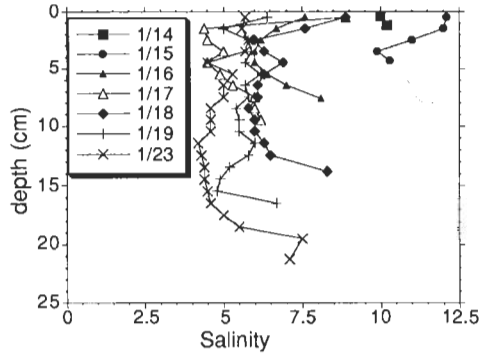

Figure 2. Salinity profiles from the indoor pit facility during the CRREL'92 experiment.

screen for the succeeding three lifts. This resulted in the lower density values for these.

3.3.2. *CRRELEX'90 outdoor pond measurements*

Measurements of the ice characteristics during the 1990 CRRELEX campaign were limited to surface roughness measurements (addressed in §4) and air and ice surface temperatures, as well as ice thickness. For the measurements shown in this paper the air temperature was -2 to $-3°$ C, and the ice surface temperature was $-1{\cdot}5°$ C. The ice had grown to a thickness of 20 cm when these measurements were taken.

4. Surface roughness measurements

The accurate computation of surface roughness characteristics is vital in determining the dominant backscatter mechanism for sea ice. We have used two

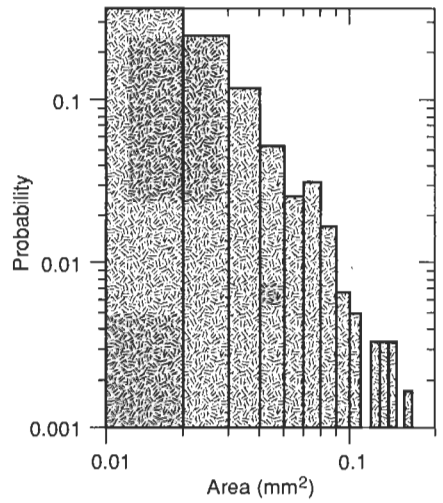

Figure 3. The brine inclusion size distribution for a saline ice thin section (from Perovich and Gow 1992).

Table 2. Ice section parameters at three depths.

	10 mm	30 mm	80 mm
Salinity (‰)	6·7	4·2	9·4
Temperature (°C)	−3·12	−2·76	−1·79
Brine volume fraction	0·109	0·077	0·263
Mean area (mm^2)	0·036	0·022	0·045
Mean axis length (mm)	0·25	0·24	0·32
Circularity	30·5	28·1	29·3

techniques for measuring surface roughness. One involves photographing thick ice sections and the other utilizes a wood grain gauge to obtain a contour of the ice surface. The first technique requires one to cut thick sections from the ice sheet and photograph the profile against a centimetre grid. These photographs are scanned into a computer and magnified to show detail. The surface profile function is obtained by using a mouse and a standard graphics program. This surface profile is used to compute the rms surface roughness and the autocorrrelation function for the surface. The correlation length is determined from the autocorrelation function. With the second method we obtained a surface profile by pressing a wood grain gauge onto the ice surface and photographing the gauge against a centimetre grid. This photograph is also scanned into a computer and the roughness statistics are obtained in the same manner as the method for the thick section photographs. This technique was used to characterize the surfaces for both the CRREL'90 and '92 experiments, and the parameters are listed in table 3. The CRREL'90 results are from a 20-cm-thick saline ice sheet and the 1992 results are from a 12 cm-thick ice sheet.

Figure 4 shows an autocorrelation function obtained from a thick section photograph, taken during CRRELEX'90. This ice had an rms surface height of 1·36 mm. Figure 5 shows an autocorrelation obtained from a grain gauge photograph, taken during the International Arctic Ocean Expedition (IAOE'91) field experiment (Beaven and Gogineni 1994). This autocorrelation is from a multi-year ice surface, which typically has higher surface roughness than simulated sea ice. In this case the rms surface height was 4·2 mm. This case has a much higher signal-to-noise ratio (SNR) than the case shown in figure 4. From these we observe that SNR has a direct effect on the determination of correlation length.

4.1. *Effects of noise on surface roughness parameter estimates*

Like any measurement, the surface roughness measurements are affected by noise. In this case the noise can be induced by a number of factors. These include digitization error, altering of the surface obtained with thick sections caused by

Table 3. Surface roughness computations.

	CRREL'90	CRREL'92
Rms surface height (mm)	1·36	0·684
Correlation length (cm)	1·76	1·4

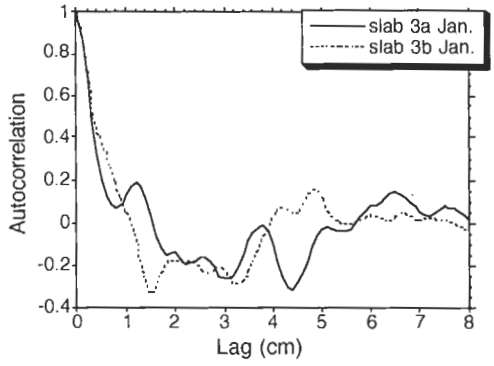

Figure 4. Autocorrelation function from CRRELEX'90. The rms surface roughness was 1·36 mm and the correlation length was 1·76 cm.

cutting, and inaccurate profiling with the grain gauge. Recently, Jezek *et al.* (1993) have taken comb gauge measurements and also quantified the contribution of noise. The signal-to-noise ratio (SNR) for their measurements ranged from 0 dB to about 10 dB. To observe the effect of noise on surface roughness and correlation length measurements we performed a simple simulation.

We simulated the effects of SNR on the estimation of the correlation length of a rough surface. We generated a rough surface with an exponential autocorrelation function of 1000 samples with a correlation length of 11·3 cm and an rms surface height of 0·2 mm. We then added white Gaussian noise with different variances to the original rough surface samples and created seven signals with SNRs ranging from from 0 to 6 dB. The effects of the SNR on the estimation of the correlation length are presented in table 4 and are illustrated in figure 6.

This simulation shows that with an SNR of 0 dB an error of as much as 60·8 per cent can occur in the estimation of correlation length. This means that the actual correlation length may be over 2·5 times larger than what is measured. This error can have a significant impact on theoretical model predictions and can cause

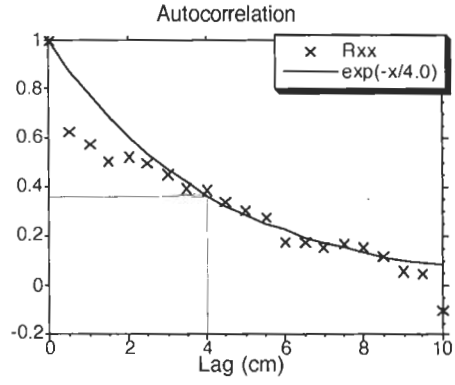

Figure 5. Autocorrelation function from IAOE'91. The rms surface roughness was 4·2 mm and the correlation length was 4 cm.

Table 4. Theoretical effect of SNR on surface roughness measurements.

SNR (dB)	Correlation length (cm)	Percentage error (%)
∞	11·3	0
6	9·86	12·7
4	9·21	18·5
2	8·03	28·9
0	4·43	60·8

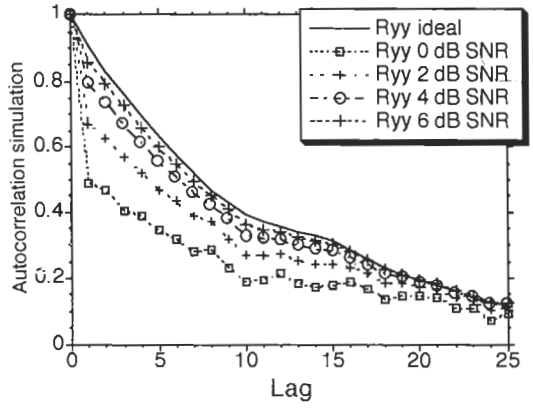

Figure 6. The simulated effect of SNR on correlation function estimates.

misinterpretation of the backscatter data as well as the scattering mechanisms involved. These results are particularly applicable for experiments on the smooth ice surfaces grown at CRREL.

5. Data processing

The step-frequency radar systems described in §2 were used to measure the power backscattered from saline ice. This is then used to compute σ^0 with the narrow-beam approximation of the radar equation as

$$\sigma^{\circ} = \frac{P_r \sigma_{cal} R^4 P_{dical}}{P_{cal} R_{cal}^1 A P_{dl}} \tag{1}$$

Here P_r is the power returned from the distributed target and P_{cal} is the power returned from a calibration target of known radar cross section σ_{cal}. The parameters P_{dlcal} and P_{dl} are the delay line readings taken at the time of calibration and the time of the field measurement, respectively. The range to the distributed target is R, A is the area illuminated by the antenna, and R_{cal} is the range to the calibration target.

The narrow-beam approximation holds for cases in which the antenna has a narrow beamwidth. When obtaining scatterometer data, a wide-beam antenna is often used. This type of antenna may be used for several reasons such as cost constraints, size constraints and satisfaction of the far-field criterion. In cases where

the scattering coefficient does not vary significantly with angle the use of a wide-beam antenna does not cause a large error when the narrow-beam approximation is used in calculating σ°. However, when the surface under investigation is relatively smooth, the narrow-beam approximation can cause significant errors in the σ° calculation, particularly near normal incidence. Thus, a beamwidth correction algorithm introduced by Wang and Gogineni (1991) was applied to data taken during the CRREL 1990 and 1992 experiments. Any data presented here that have been beamwidth-corrected are noted as such.

In addition to antenna pattern effects, radar measurements are subject to other systematic errors. These errors include the frequency response of the system and coupling effects in the antennas. Real antennas have a finite ratio of co-polarized signal to cross-polarized signal, resulting in some energy being transmitted as a vertically-polarized wave when the antenna is horizontally polarized and vice versa. In this paper we will refer to this ratio as the polarization ratio of the system. Ideal systems have infinite polarization ratio. Signal leakage due to a system with a finite polarization ratio can cause significant errors in measuring backscatter, particularly for cross-polarized measurements. To reduce the effect of signal leakage due to finite polarization ratio a vector calibration technique was applied to the CRREL'90 data set. The calibration required the use of three calibration targets: a sphere, a diplane in two orientations, and a Luneburg lens. The technique was based on that of Riegger and Wiesbeck (1989), which was used to calibrate hard targets, but here was applied to returns from saline ice.

The vector calibration technique is based on the assumption that the measured reflection coefficient of an object is a linear combination of the reflection coefficients from all four polarizations. The measured reflection coefficient at VV polarization is given by,

$$s_{vv}^m = c_{11}s_{vv}^0 + c_{12}s_{hh}^0 + c_{13}s_{vh}^0 + c_{14}s_{hv}^0, \tag{2}$$

where s_{vv}^0, s_{hh}^0, s_{vh}^0, and s_{hv}^0 are the true reflection coefficients for the target for each polarization combination. For a set of four linear polarization combinations there are three additional equations similar to (2). The set of four equations can be constructed as the matrix equation,

$$\begin{bmatrix} s_{vv}^m \\ s_{hh}^m \\ s_{vh}^m \\ s_{hv}^m \end{bmatrix} = \begin{bmatrix} c_{11} & c_{12} & c_{13} & c_{14} \\ c_{21} & c_{22} & c_{23} & c_{24} \\ c_{31} & c_{32} & c_{33} & c_{34} \\ c_{41} & c_{42} & c_{43} & c_{44} \end{bmatrix} \cdot \begin{bmatrix} s_{vv}^0 \\ s_{hh}^0 \\ s_{vh}^0 \\ s_{hv}^0 \end{bmatrix}. \tag{3}$$

The 4 by 4 matrix is called the calibration matrix, $\bar{C}$. The diagonal terms are due to the frequency response of the components in the system. The off-diagonal terms are due to signal leakage caused by the finite polarization ratio of the system. The coefficient c_{32}, for example, accounts for the contribution of the HH component of the backscatter when measuring the VH component. The vector calibration was accomplished by measuring the return from three calibration targets and using these to estimate $\bar{C}$. The details of the calibration technique can be found in Beaven (1992) and Beaven *et al.* (1991).

The vector calibration results in a reduction of 10 to 20 dB in the cross-polarized measurements at C band as demonstrated in figures 7 and 8. Here we show σ° as a

function of angle for simple scalar calibration and for the vector calibration. For K_u-band measurements the vector calibration demonstrated that the error caused by signal leakage due to finite polarization ratio was as much as 15 dB. The vector calibration was used on all the data obtained during CRRELEX'90.

6. Presentation of experimental results

6.1. *Ice growth results*

Figures 9 and 10 illustrate the variation of the beamwidth-corrected scattering coefficient with ice thickness for various angles of incidence. Both *VV* and *HH* polarizations are included with thicknesses ranging from 0·5 to 12 cm. These demonstrate that the co-polar backscatter decreases by about 12 dB at normal incidence as the ice sheet grows from 0·5 cm to 12 cm. This is accompanied by a 12 to 14 dB increase in backscatter at incidence angles of 25° and 45°. Most of the increase occurs during the first 8 cm of growth and the backscatter then levels off.

We believe that this change in backscatter is caused by a decrease of the bulk dielectric constant as ice forms and grows. This is accompanied by an increase in surface roughness due to brine expulsion. Both effects contribute to the decrease in backscatter at normal incidence, whereas the latter causes an increase in scattering at large incidence angles.

6.2. *Snow-covered ice results*

Figure 11 shows the change in the sea ice signature as a result of the introduction of the snow layers for *VV* and *HH* polarization at 0°, 15° and 45° incidence angles. It is interesting to observe that the scattering coefficient changes by as much as 17 dB from the bare ice case to the 2·5-cm snow cover case while the scattering coefficient changes by no more than 2 or 3 dB after the addition of two more snow layers. Figure 12 shows a comparison in normal incidence backscatter between the 12-cm snow cover and 12-cm bare ice conditions. These data are the result of 10–12 independent measurements taken across the ice (or snow-covered ice) sheet. This demonstrates that in addition to the decrease in normal incidence backscatter there is an increase in the variation of the backscatter.

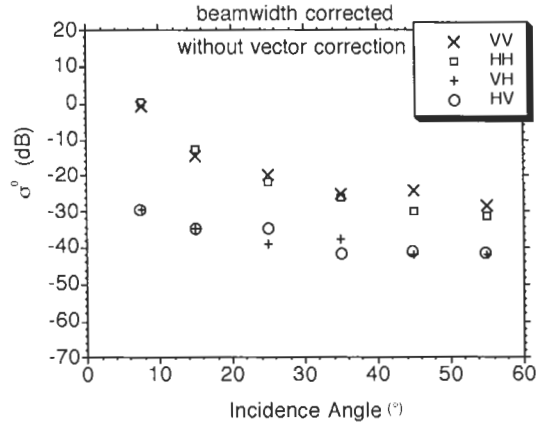

Figure 7. Backscattering coefficients from a 20-cm thick saline ice sheet at *C* band using scalar calibration. The cross-polarized measurements show the effect of signal leakage due to the finite polarization ratio of the system.

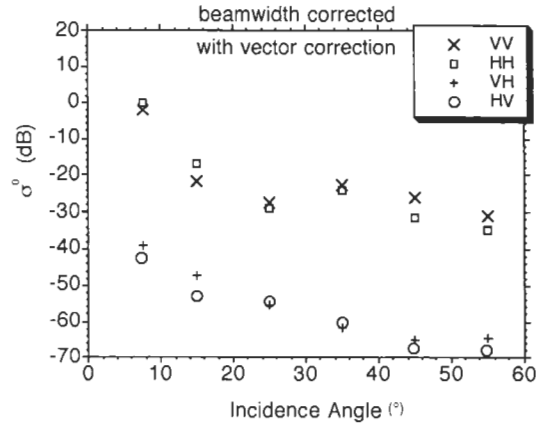

Figure 8. Backscattering coefficients from a 20-cm thick saline ice sheet at *C* band using the complex vector calibration. These measurements show the improvement in the dynamic range of the measurement.

6.3. *Deep snow-covered ice*

After completing the snow-cover experiments with a 12-cm snow layer we piled 21 cm of snow in a small area of the CRRELEX indoor pit. This snow pile was deep enough so that the return from the air-snow interface was resolvable from the snow-ice interface. The resolution of the radar in snow is approximately 11 cm. First, we placed a metal plate on top of the snow pile and measured the return at normal incidence. This provided a 'range marker' to the snow surface. Then we removed the plate and measured the backscatter at normal incidence from the deep snow-covered ice. The result of this experiment is shown in figure 13. Here we see that at the position of the metal plate return, the return from the snow-covered ice is negligible. The peak of the snow-covered ice return occurs 20 cm further in range. This corresponds to the snow-ice interface. This result clearly demonstrates that the

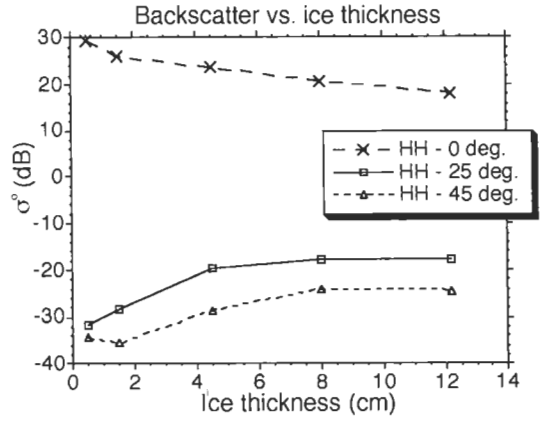

Figure 9. K_u-band backscattering coefficients from saline ice as a function of thickness for *HH* polarization at several angles. (Data are beamwidth-corrected.)

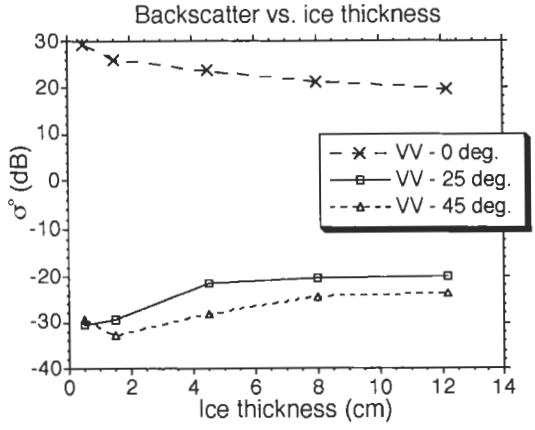

Figure 10. K_u-band backscattering coefficients from saline ice as a function of thickness for VV polarization at several angles. (Data are beamwidth-corrected.)

return from the air-snow interface is significantly lower than the return from the snow-ice interface. A significant contribution due to snow volume scatter would cause a broadening of the returned power. We did not observe any significant broadening, therefore we conclude the snow volume scatter contribution was negligible.

7. Comparison to scattering theory

7.1. *Surface scattering*

The scattering from a surface consists of two components: a coherent and an incoherent component. The total surface backscatter is the sum of the incoherent and coherent components. For relatively smooth surfaces the coherent component dominates near normal incidence. For very rough surfaces the incoherent component dominates. The coherent component of the scattering must be considered when the rms surface height is smaller than $\lambda/4$ (Ulaby *et al.* 1986). The rms surface roughness is smaller than $\lambda/10$ for K_u band and $\lambda/25$ for C band in the highest rms

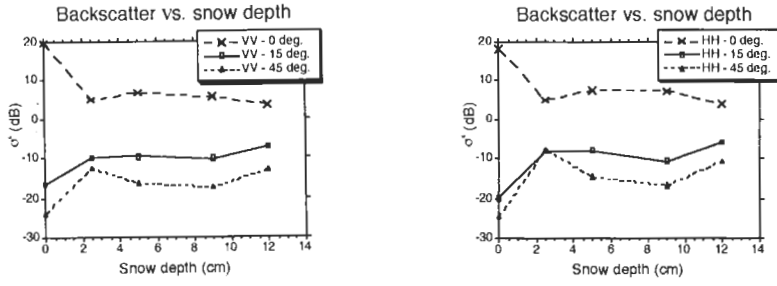

Figure 11. K_u-band backscattering coefficients versus snow depth for 0°, 15° and 45° incidence. The left plot shows the VV scattering coefficient and the right shows the HH scattering coefficient. The underlying ice was 12cm thick. (Data are beamwidth-corrected.)

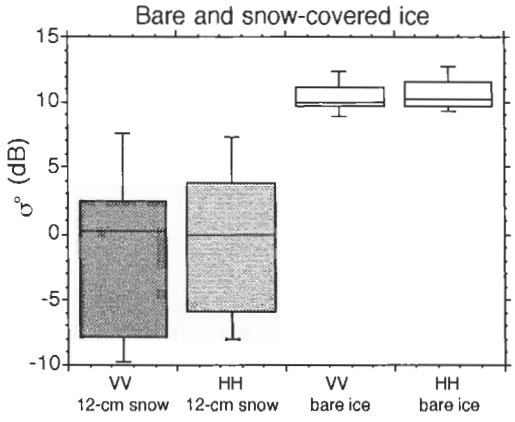

Figure 12. K_u-band backscatter coefficient variation at 0° incidence for snow-covered and bare saline ice. The middle bar indicates the median value. The upper and lower ends of the box indicate ±25 per cent points (half of the measurements fall in this range), and the extended lines indicate the ±45 per cent points of the distribution.

roughness case for the CRREL experiments. Because of this, the coherent component of the scattering must be considered here.

Several theories to solve the incoherent scattering from rough surfaces exist in the literature, including the integral equation method (IEM) (Fung *et al.* 1992), the Kirchhoff model (Rice 1951), the two-scale model (Wu and Fung 1972), and the small perturbation method (Ulaby *et al.* 1982). An advantage of the IEM is that it is valid for all frequencies, whereas the other techniques are valid only for high- or low-frequency regimes.

The coherent component of the backscatter is due to the direct reflection at the surface and dominates near nadir. Also called the specular component, it can be described as (Ulaby *et al.* 1982)

$$\sigma_c = \pi k_1 |a_0|^2 \delta(q_x)\delta(q_v), \tag{4}$$

where k_1 is the wave number in the first medium, usually free space, and a_0 is

$$a_0 = -2R_{h0}\,(\cos\theta) \tag{5}$$

for *HH* polarization and

$$a_0 = -2R_{v0}\,(\cos\theta) \tag{6}$$

for *VV* polarization. Here R_{h0} is the perpendicular (horizontal) polarization Fresnel reflection coefficient and R_{v0} is the parallel (vertical) polarization Fresnel reflection coefficient. Due to the Dirac delta functions, $\delta(q_x)$ and $\delta(q_v)$, the coherent component exists only for 0° incidence angle in the ideal case. When using finite-beam antennas a first-order solution to the contribution due to the coherent component of the scattering is, (Fung and Eom 1983)

$$\sigma^0_{ppc} \cong \frac{\Gamma_p(\theta)}{B^2} \exp(-4k^2\sigma_h^2) \exp(-\theta^2/B^2), \tag{7}$$

where p is the polarization, θ is the incidence angle, Γ_p is the reflection coefficient for polarization p (either H or V), and B is given by

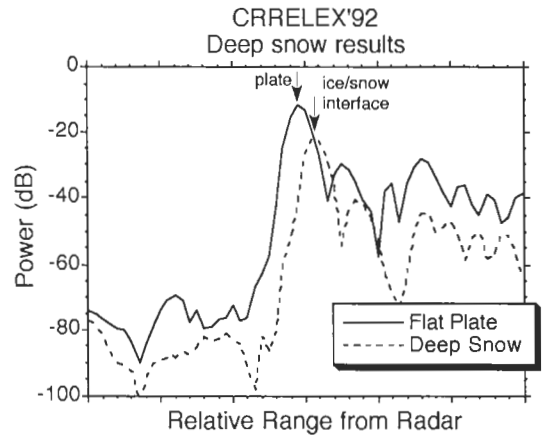

Figure 13. Comparison of K_u-band radar returns at 0° incidence angle from a 21-cm snow pile and a metal plate on top of the snow pile. The ice thickness was 12 cm. This demonstrates that the return from snow-covered saline ice is dominated by scattering from the snow-ice interface.

$$B^2 = \frac{1}{(kR_0\beta)^2} + (\beta/2)^2. \tag{8}$$

The one-sided, 3-dB beamwidth of the antennas is β and the range to the scatterer is R_0.

We use the above approximation to compute the coherent portion of the backscatter, and the IEM for computing the non-coherent component of the theoretical surface scatter from the surface parameters measured during the CRRELEX campaigns. The details of this technique can be found in (Fung *et al.* 1992).

7.2. *Volume scattering theory*

Since we have a lossy ice layer the optical depth is large. Thus, the ice layer is treated as a half-space. To model volume scattering from a half-space we used the first-order Radiative Transfer Model using the Rayleigh phase matrix (Fung and Eom 1982, Chandrasekhar 1960), which has two parameters, spectral albedo and optical depth. The spectral albedo is adjusted to fit the data, but it falls within the range of theoretical spectral albedo calculations from § 3.3.1, which are based on the measured ice properties.

7.3. *Comparison of measurements and theory*

7.3.1. *Bare saline ice*

Using the surface roughness parameters measured as discussed in § 4, we computed the surface component of the backscatter. All parameters used in the model are shown in table 5. The permittivity values chosen for C and K_u bands are 3·5–j0·22 and 3·45–j0·2, respectively. These are reasonable values for ice of the salinity measured at CRREL (Arcone *et al.* 1986). These parameter values are used for computing both co-polarized and cross-polarized scattering at both frequency bands. We added the coherent component from (7) to account for antenna pattern effects around normal incidence. Figure 14 and figure 15 show model predictions

and measured data for co-polarized and cross-polarized scattering, respectively. To understand the impact due to volume scattering in these figures we show both the total scattering (surface plus volume) and the volume scattering component by itself. The volume scattering term is based on Rayleigh scattering with a spectral albedo of 0·002 at *C* band and 0·003 at K_u band. From figure 14 we see that there is excellent agreement between the measurement and surface scattering theory for both frequencies. The angular trends are also in very good agreement. The coherent portion of the scattering accounts for the increase in backscatter below 15°. The fact that the measurements at *VV* and *HH* do not show much separation at large angles of incidence appears to indicate that some volume scattering effect due to inhomogeneities in the ice is present. Clearly, the volume scattering effect is negligible for small and intermediate incidence angles. At large angles the volume scattering contributes to the narrowing of the difference in backscatter between *VV* and *HH* polarizations and slightly increases the level of backscatter. The volume scatter at K_u band is higher than at *C* band because of the larger spectral albedo. However, the normalized surface roughness is higher at K_u band, causing the surface scatter component to be higher as well.

To compare theory with CRRELEX'92 measurements the case under consideration is a 12 cm-thick saline ice layer with a normalized rms height of 0·19 and a correlation length of 3·92 at 13·4 GHz. The surface correlation is again closely exponential. The ice relative permittivity is 3·38–j0·23. The parameters used in the model are shown in table 6. When we choose a spectral albedo of 0·0015 we obtain an excellent fit as shown in figure 16. The optical depth is so thick that the scattering acts as if it is from a half-space. In figure 16 we show the surface contribution from air-ice interface and volume scattering in addition to the total scattering. It is observed that for small and intermediate incidence angles the surface scattering is dominant, leading to higher scattering from *VV* than *HH*. At large incidence angles volume scattering begins to make a contribution, resulting in narrowing the spacing between *VV* and *HH* polarizations, but not increasing the level of the backscatter by more than 3 dB.

7.3.2. *Snow-covered saline ice*

The addition of the snow cover caused a dramatic change in the backscatter as evidenced by figures 11 and 12. The normal incidence backscatter decreased by 12 to 15 dB for beamwidth-corrected data. This was accompanied by an increase in backscatter at larger incidence angles. These changes may be due to a roughening of the surface at the snow-ice interface. The new surface caused by brine wicking into

Table 5. Model parameters for CRRELEX'90 bare saline ice.

	C band	K_u band
Rms roughness, σ_h	1·36 mm	1·36 mm
Correlation length, L_c	1·76 cm	1·76 cm
Normalized roughness, $k\sigma_h$	0·152	0·38
Normalized correlation, kL_c	1·95	4·99
Dielectric constant, ε_r	3·5–j0·22	3·45–j0·2
Optical depth	half-space	half-space
Spectral albedo	0·002	0·003

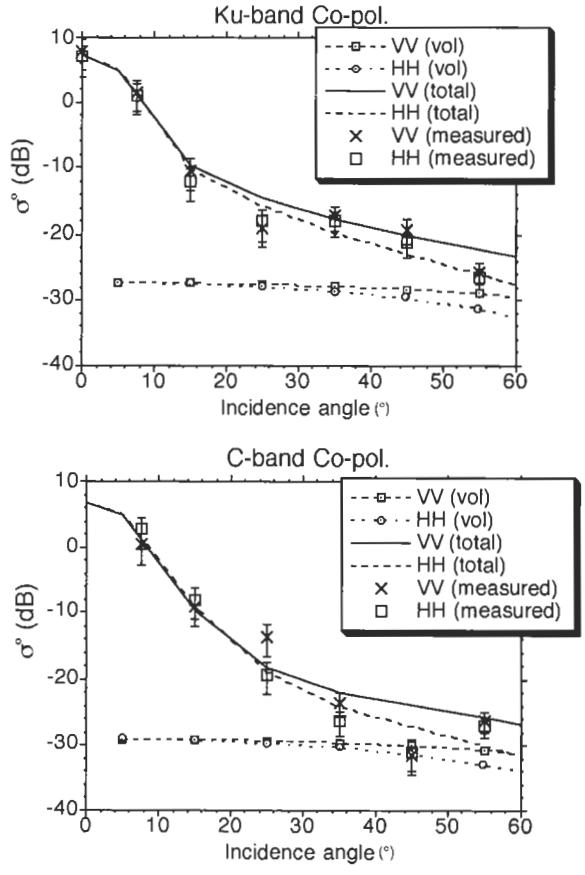

Figure 14. Comparison of copolarized measurements and theory at K_u band (top) and C band (bottom) for the 20-cm thick bare saline ice sheet investigated during CRRELEX'90.

the snow layer is difficult, if not impossible, to characterize with the surface roughness measurement techniques shown in §4. To obtain an estimate of the surface roughness we used the normal incidence σ°, along with the coherent component (7), to estimate the rms roughness. Before the introduction of the snow layer, the normal incidence σ° was 10·5 dB (without beamwidth correction). The mean σ° after the application of snow layers was 3 dB at normal incidence. This decrease can be accounted for by an increase in normalized rms surface height ($k\sigma_h$) from 0·19 to 0·33. We used a proportionate increase in normalized correlation length (kL_c) from 3·92 to 6·8 in the total scattering model (IEM surface plus Rayleigh volume), and the results are shown in figures 17 and 18, for the 12-cm and 5-cm snow cover cases. Because of the general agreement between measured and theoretical σ°, we observe that the roughening of the surface can account for the decrease in backscatter at normal incidence and its increase at higher incidence angles. This modelling supports the argument that the brine wicking into the snow layer causes a roughening of the surface at the snow-ice interface that alters the radar signature of the sea ice. Another support for the roughening-effect argument is the fact that the

backscattering at nadir decreased upon the addition of the first layer of snow, indicating a rougher surface, and the additional snow layers did not significantly alter the signature. This theory however does not account for the *HH* return being higher than the *VV* return at some incidence angles. The difference between *VV* and *HH*, however, is less than the experimental error (+1·4 dB, −2·3 dB at high angles) because only three independent measurements could be made for the snow-covered ice sheet due to the size of the experiment site.

The fact that the *HH* backscatter is higher than for *VV* at some incidence angles may be due to the change in dielectric contrast at the snow-ice interface. Before adding the snow layer the interface of importance is the ice-air interface. The ratio of the dielectric constant of the ice with respect to the air (dielectric contrast) is between 3 and 4. When the snow layer is added and brine wicks into the snow the dielectric constant of the ice surface increases. To investigate the possible effect due to an increase in dielectric contrast we use the same roughness parameters as in the bare saline ice case and change the dielectric constant of the ice surface to fit the data. In figure 19 we show the same ice with a 12-cm thick snow cover. In this case all ice

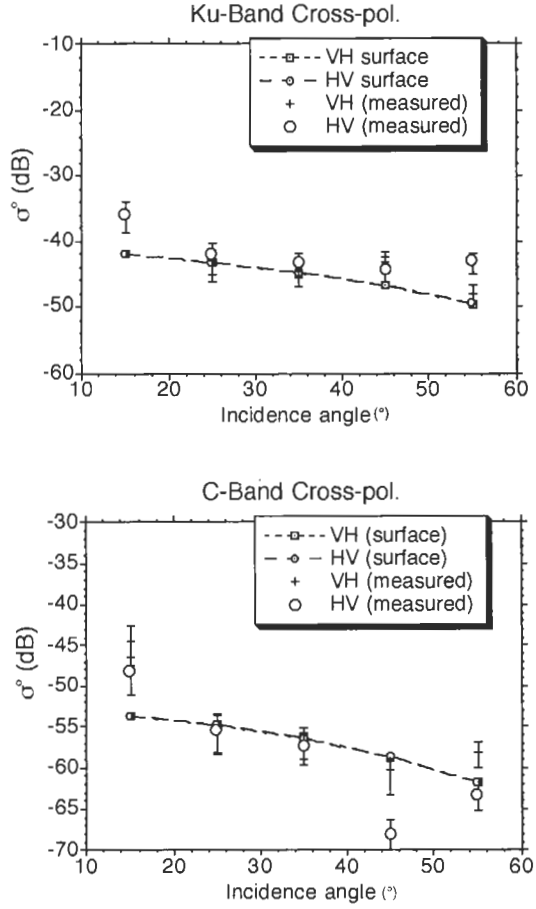

Figure 15. Comparison of cross-polarized measurements and theory at K_u band (top) and C band (bottom) for the 20-cm thick bare saline ice sheet investigated during CRRELEX'90.

Table 6. Model parameters for CRRELEX'92 bare saline ice.

	K_u band
Rms roughness (σ_h)	0·684 mm
Correlation length (L_c)	1·4 cm
Normalized σ_h ($k\sigma_h$)	0·19
Normalized L_c (kL_c)	3·92
Dielectric constant, ε_r	3·38–j0·23
Optical depth	4·3
Spectral albedo	0·0015

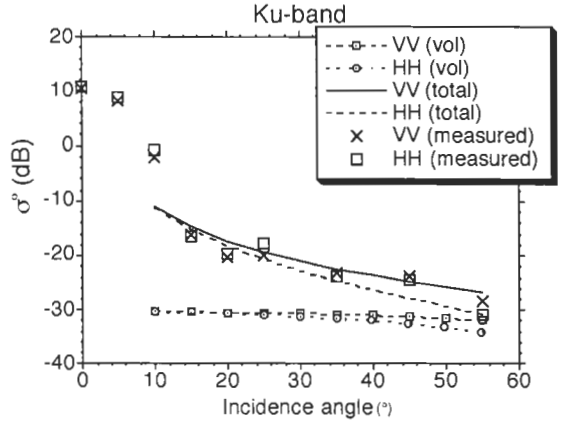

Figure 16. Comparison of copolarized measurements and theory at K_u band for the 12-cm bare saline ice sheet investigated during CRRELEX'92. The coherent component is not included here for the model computations.

surface parameters remain unchanged except for the ice permittivity, the real part of which is increased from 3·38 to 9·38 to account for the wicking effect of the brine. (The real part of the dielectric constant of pure sea water is around 40 at K_u band.) In this modelling we increased only the real part of the dielectric constant. It is possible to obtain a similar fit by changing the dielectric constant to 5·4–j4·95 (Fung *et al.* 1994). Although the value of dielectric constant required to obtain the fit is not unique, the dielectric constant must be increased to obtain the fit. Note that because snow has a relative permittivity of 1·67–j0·00026, the air-snow interface does not contribute much to the total backscatter. Figure 20 shows the same results without the air-snow surface scattering term. It is clear from figure 20 that there is good agreement between the theoretical model and measured data. To demonstrate what happens if we reject the idea that there is wicking of the brine by keeping the ice permittivity the same as before the snow cover is applied, then we obtain the fit shown in figure 21. In this case the model prediction is clearly significantly lower than the measurements, especially at lower angles of incidence where surface scattering should dominate the return. At large angles the backscatttered signal is

primarily due to volume scattering and therefore the general agreement is not affected very much. An additional point that justifies the presence of wicking is that when snow is present *HH* is higher than *VV*. This comes about because of surface-volume interaction resulting from scattering by the snow layer and snow-ice interface. Such an interaction only boosts the *HH* return and not the *VV* return because of the Brewster angle effect. Finally, we further justify our modelling interpretation by considering the same ice with a 5-cm thick snow cover. In this case we only change the optical depth by the same proportion as the change in physical depth; i.e., from 0·05 to 0·021. All other model parameters remain the same as those shown in figure 20. The resulting fit is given in figure 22. Again, good agreement is obtained.

In summary, we believe that surface scattering is the dominant scattering mechanism for bare saline ice at small and intermediate angles of incidence. At large incidence angles, volume scattering can narrow the difference between *VV* and *HH* returns, but it only increases the level by 2 to 3 dB. For snow-covered sea ice, brine wicking occurs, causing an increase in permittivity discontinuity and surface roughening at the snow-ice interface. This effect, plus the effect of the surface-volume interaction, causes *HH* backscattering to be higher than *VV* backscattering in the snow-covered case, compared to the bare saline ice case.

8. Conclusions

We performed measurements under controlled conditions to determine the mechanisms that govern radar backscatter from young saline ice. These measurements utilized a vector calibration to improve the quality of cross-polarized measurements. This type of calibration is necessary whenever dual antenna systems or antennas without high polarization ratios are used. We performed detailed ice characterization, particularly the brine pocket size distribution and the surface

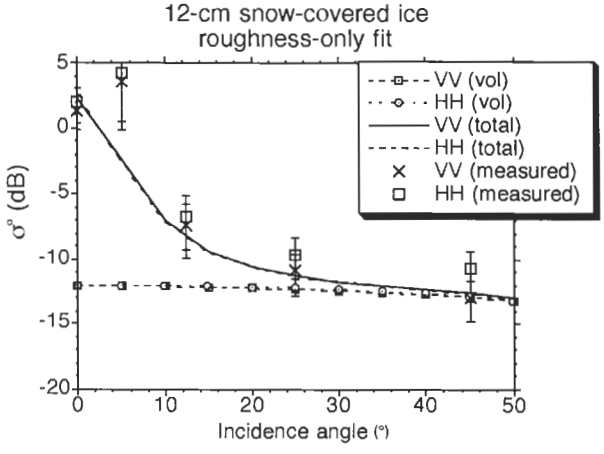

Figure 17. Comparison of K_u-band backscatter measurements from snow-covered saline ice with IEM surface and Rayleigh volume scattering models. The ice thickness was 12 cm and the snow depth was 12 cm. The fit was obtained by finding the roughness required to reduce the return at 0° assuming the coherent component dominates there. This shows that an increase in roughness due to brine wicking into the snow layer can cause the changes observed with the introduction of the snow layer.

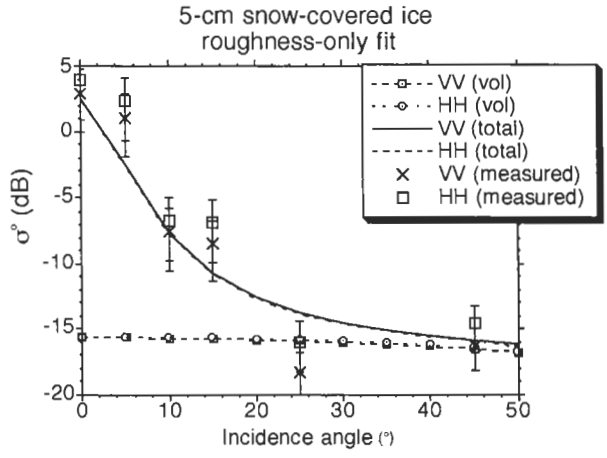

Figure 18. Comparison of K_u-band backscatter measurements from snow-covered saline ice with IEM surface and Rayleigh volume scattering models, using the same surface roughening assumption as figure 17. The ice thickness was 12 cm and the snow depth was 5 cm.

roughness. These are the key parameters that are used in scattering models for sea ice. We used these physical data in existing scattering models to infer which mechanisms are responsible for backscatter from young saline ice and snow-covered saline ice. The models used parameters measured directly from the ice characteristics, and assumed parameters fell within the limits defined by computations based

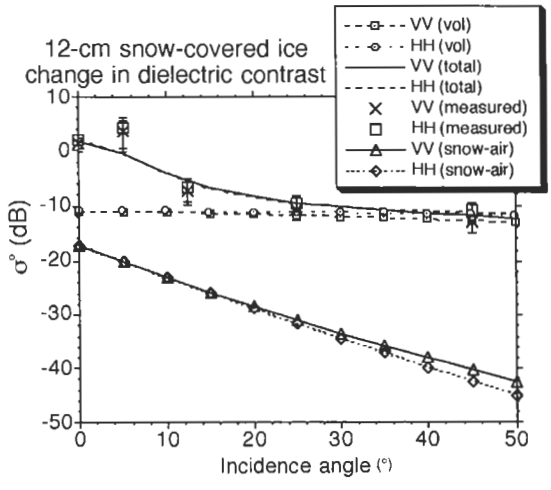

Figure 19. Comparison of K_u-band backscatter measurements from snow-covered saline ice with IEM surface and Rayleigh volume scattering models. The ice thickness was 12 cm and the snow depth was 12 cm. This demonstrates that an increase in the dielectric contrast (with an increase in roughness due to change in wave number) can account for the change in backscatter with the introduction of a snow layer. Scattering from the snow-air interface is well below the total scattering.

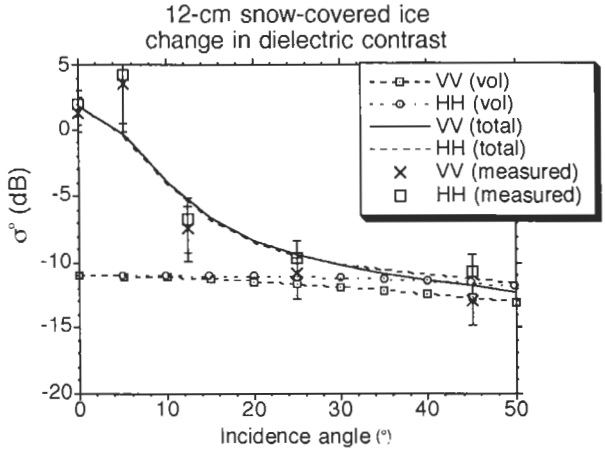

Figure 20. Comparison of K_u-band backscatter measurements from snow-covered saline ice with IEM surface and Rayleigh volume scattering models. The ice thickness was 12 cm and the snow depth was 12 cm. This demonstrates that an increase in the dielectric contrast (with an increase in roughness due to change in wave number) can account for the change in backscatter with the introduction of a snow layer. Here the snow-air contribution is not shown.

on measured properties. We found that at *C* band the surface scatter dominates the return for low and moderate incidence angles. At high incidence angles the separation in backscatter between the *VV* and *HH* returns is reduced by the volume scattering component. At K_u band the results are similar, with surface scattering being the dominant scattering mechanism at low and moderate incidence angles. At

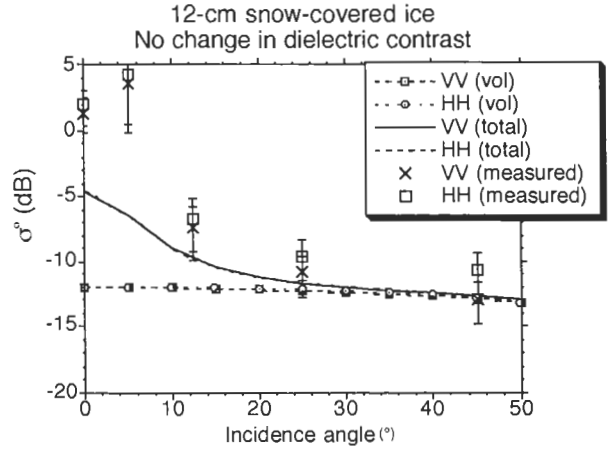

Figure 21. Comparison of K_u-band backscatter measurements from snow-covered saline ice with IEM surface and Rayleigh volume scattering models. The ice thickness was 12 cm and the snow depth was 12 cm. The theory in this case does not account for the change in dielectric constant caused by brine wicking.

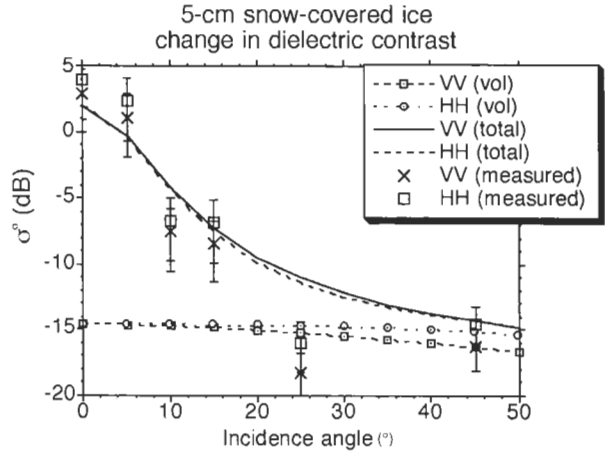

Figure 22. Comparison of K_u-band backscatter measurements from snow-covered saline ice with IEM surface and Rayleigh volume scattering models. The ice thickness was 12 cm and the snow depth was 5 cm. This demonstrates that an increase in the dielectric contrast (with an increase in roughness due to change in wave number) can account for the change in backscatter with the introduction of a snow layer.

high angles the volume scattering component acts to support the level of backscatter as well as to decrease the separation between *VV* and *HH* scattering.

We have shown how the backscatter changes in the early stages of ice growth at several incidence angles. The growth of the ice sheet results in a change in bulk dielectric constant (Onstott 1992). We've demonstrated the effect of this changing dielectric constant on the backscatter at 0°, 25° and 45° incidence angles. This dependence may be exploited to determine ice thickness on a larger scale, using a technique similar to that used for estimating soil moisture (Ulaby *et al.* 1982). This can be accomplished in a practical manner if the range of incidence angles are selected such that σ° is independent of the surface roughness.

For snow-covered saline ice we investigated two possibilities to explain the change in backscatter: roughening of the surface at the snow-ice interface and the change in dielectric constant contrast at the surface. We believe that the roughening of the snow-ice interface, caused by brine wicking into the snow layer, causes the increase in backscatter. This is accompanied by a change in the dielectric contrast at the interface. Each of these effects causes the backscatter to increase at most incidence angles. The roughening effect causes the backscatter to drop significantly at nadir. These changes take place with the introduction of a thin snow layer of 2·5 cm. The addition of more snow does not result in significant changes in the backscatter. These snow-cover results confirm observations made during previous experiments in which urea ice was used as a saline ice simulant (Lytle *et al.* 1993).

Acknowledgments

The authors would like to thank Mr Terry Tucker, Dr Al Lohanick, and Mr John Govoni of CRREL for their support during the experiments and for allowing us to conduct experiments on ice sheets grown on the lower pond. This work was

funded by an Office of Naval Research (ONR) Fellowship and ONR grant # N00014-89-J-1456.

References

ARCONE, S. A., GOW, A. J., and MCGREW, S., 1986, Microwave dielectric, structural and salinity properties of simulated sea ice. *I.E.E.E. Transactions on Geoscience and Remote Sensing*, **24,** 832–839.

BEAVEN, S. G., 1992, Radar Backscatter Measurements from Simulated Sea Ice and Arctic Sea Ice During the Fall Freeze-up. M.S. Thesis, University of Kansas.

BEAVEN, S. G., and GOGINENI, S. P., 1994, Shipborne radar backscatter measurements from arctic sea ice during the fall freeze-up. *Remote Sensing Reviews*, **9,** 3–25.

BEAVEN, S. G., GOGINENI, S. P., TJUATJA, S., FUNG, A. K., and BREDOW, J., 1991, Radar backscatter from saline ice: measurements and comparison of measurements with theory. *Proceedings IGARSS'91*, **2** (Piscataway, New Jersey: I.E.E.E. Press), pp. 425–428.

CHANDRASEKHAR, S., 1960, *Radiative Transfer* (New York: Dover).

FUNG, A. K., and EOM, H. J., 1982, Application of a combined rough surface and volume scattering theory to sea ice and snow backscatter. *I.E.E.E. Transactions on Geoscience and Remote Sensing*, **GE-20,** 528–536.

FUNG, A. K., and EOM, H. J., 1983, Coherent scattering of a spherical wave from an irregular surface. *I.E.E.E. Transactions on Antennas and Propagation*, **AP-31**, 68–72.

FUNG, A. K., LI, Z., and CHEN, K. S., 1992, Backscattering from a randomly rough dielectric surface. *I.E.E.E. Transactions on Geoscience and Remote Sensing*, **GE-30,** 356–369.

FUNG, A. K., TJUATJA, S., BEAVEN, S., GOGINENI, S. P., JEZEK, K., GOW, A. J., and PEROVICH, D. K., 1994, Modeling interpretation of scattering from snow-covered sea ice. *Proceedings IGARSS'94*, **1** (Piscataway, New Jersey: I.E.E.E. Press), pp. 617–620.

GOW, A. J., 1986, Optical characterization of sea ice structure using polarized light techniques. *Proceedings of the Informational Society of Optical Engineering*, **637,** 264–271.

IIZUKA, K., and FREUNDORFER, A. P., 1984, Step-frequency radar. *Journal of Applied Physics*, **56,** 2572–2583.

JEZEK, K. C., ZABEL, I. H. H., and GOGINENI, S. P., 1993, Sea ice roughness: simulation and characterization. Byrd Polar Research Center internal report, The Ohio State University, 1993.

LOVE, A. W., 1962, The diagonal horn antenna. *The Microwave Journal*, **5,** 117–122.

LYTLE, V. I., JEZEK, K. C., HOSSEINMOSTAFA, R., and GOGINENI, S. P., 1993, Laboratory backscatter measurements over urea ice with a snow cover at K_u band. *I.E.E.E. Transactions on Geoscience and Remote Sensing*, **31,** 1009–1016.

ONSTOTT, R. G., 1992, SAR and scatterometer signatures of sea ice. In *Microwave Remote Sensing of Sea Ice*, edited by F. D. Carsey (Washington, D.C.: American Geophysical Union), *Geophysical Monograph*, **68,** 73–104.

PEROVICH, D. K., and GOW, A. J., 1992, Towards a quantitative characterization of sea ice microstructure. *Proceedings IGARSS'92*, **2** (Piscataway, New Jersey: I.E.E.E. Press), pp. 1249–1252.

RIEGGER, S., and WIESBECK, W., 1989, Wide-band polarimetry and complex radar cross section signatures. *Proceedings of the I.E.E.E.*, **77,** 649–658.

RICE, S. O., 1951, Reflection of electromagnetic waves from slightly rough surfaces, *Communications in Pure and Applied Mathematics*, **4,** 361–378.

SWIFT, C. T., ST. GERMAIN, K., JEZEK, K., GOGINENI, S. P., GOW, A., PEROVICH, D., GRENFELL, T., and ONSTOTT, R., 1992, Laboratory investigations of the electromagnetic properties of artificial sea ice. In *Microwave Remote Sensing of Sea Ice*, edited by F. D. Carsey (Washington, D.C.: American Geophysical Union), *Geophysical Monograph*, **68,** 177–200.

TIMCO, G. W., 1980, The mechanicaal properties of saline-doped and carbamide (urea)-doped model ice. *Cold Regions Science and Technology*, **3,** 47–56.

TUCKER, W. B., III, PEROVICH, D. K., GOW, A. J., WEEKS, W. F., and DRINKWATER, M. R., 1992, Physical properties of sea ice relevant to remote sensing. In *Microwave Remote*

Sensing of Sea Ice, edited by F. D. Carsey (Washington, D.C.: American Geophysical Union), *Geophysical Monograph*, **68,** 9–28.

ULABY, F. T., MOORE, R. K., and FUNG, A. K., 1982, *Microwave Remote Sensing: Active and Passive, vol. II* (Norwood, MA: Artech House).

ULABY, F. T., MOORE, R. K., and FUNG, A. K., 1986, *Microwave Remote Sensing: Active and Passive, vol. III* (Norwood, MA: Artech House).

WANG, Q., and GOGINENI, S. P., 1991, A numerical procedure for recovering scattering coefficients from measurements with wide-beam antennas. *I.E.E.E. Transactions on Geoscience and Remote Sensing*, **25,** 778–783.

WU, S. T., and FUNG, A. K., 1972, A noncoherent model for microwave emissions and backscattering from the sea surface. *Journal of Geophysical Research*, **77,** 5917–5929.